PHYSICAL REVIEW A **93**, 053406 (2016)

Controlling electron-ion rescattering in two-color circularly polarized femtosecond laser fields

Christopher A. Mancuso,[1,*] Daniel D. Hickstein,[1] Kevin M. Dorney,[1] Jennifer L. Ellis,[1] Elvedin Hasović,[2] Ronny Knut,[1] Patrik Grychtol,[1] Christian Gentry,[1] Maithreyi Gopalakrishnan,[1] Dmitriy Zusin,[1] Franklin J. Dollar,[1,†] Xiao-Min Tong,[3] Dejan B. Milošević,[2,4,5] Wilhelm Becker,[5] Henry C. Kapteyn,[1] and Margaret M. Murnane[1]

[1]*JILA and Department of Physics, University of Colorado Boulder and NIST, Boulder, Colorado 80309, USA*

[2]*Faculty of Science, University of Sarajevo, Zmaja od Bosne 35, 71000 Sarajevo, Bosnia and Herzegovina*

[3]*Center for Computational Sciences and Graduate School of Pure and Applied Science, University of Tsukuba, Tsukuba 305-8571, Japan*

[4]*Academy of Sciences and Arts of Bosnia and Herzegovina, Bistrik 7, 71000 Sarajevo, Bosnia and Herzegovina*

[5]*Max-Born-Institut, Max-Born-Strasse 2a, 12489 Berlin, Germany*

(Received 8 January 2016; published 9 May 2016)

High-harmonic generation driven by two-color counter-rotating circularly polarized laser fields was recently demonstrated experimentally as a breakthrough source of bright, coherent, circularly polarized beams in the extreme ultraviolet and soft-x-ray regions. However, the conditions for optimizing the single-atom yield are significantly more complex than for linearly polarized driving lasers and are not fully understood. Here we present a comprehensive study of strong-field ionization—the complementary process to high-harmonic generation—driven by two-color circularly polarized fields. We uncover the conditions that lead to enhanced electron-ion rescattering, which should correspond to the highest single-atom harmonic flux. Using a velocity map imaging photoelectron spectrometer and tomographic reconstruction techniques, we record three-dimensional photoelectron distributions resulting from the strong-field ionization of argon atoms across a broad range of driving laser intensity ratios. In combination with analytical predictions and advanced numerical simulations, we show that "hard" electron-ion rescattering is optimized when the second-harmonic field has an intensity approximately four times higher than that of the fundamental driving field. We also investigate electron-ion rescattering with co-rotating fields, and find that rescattering is significantly suppressed when compared with counter-rotating fields.

DOI: 10.1103/PhysRevA.93.053406

I. INTRODUCTION

Intense femtosecond lasers can drive light-matter interactions on attosecond time scales, making it possible to coherently manipulate electron dynamics in quantum systems. The interaction of a strong laser field ($\sim 10^{14}$ W cm^{-2}) with atoms or molecules gives rise to many phenomena, including strong-field ionization (SFI) [1,2] and high-harmonic generation (HHG) [3]. In HHG, coherent beams of extreme ultraviolet and soft-x-ray light are generated [4–9], making it possible to implement coherent imaging of nanostructures with wavelength-limit spatial resolution [10–12], as well as uncovering mechanisms for spin dynamics [13–15] and energy transport [16], all using a tabletop scale apparatus. Similarly, SFI has emerged as a breakthrough technique for probing the structure and dynamics of atoms and molecules, often with angstrom spatial resolution and attosecond temporal resolution [17,18].

For linearly polarized driving laser fields, SFI and HHG are commonly described using the three-step model [19]. In this model, first the neutral atom or molecule undergoes tunnel ionization where an electron is liberated into the continuum (step 1). Next, the laser field accelerates the electron in a trajectory that depends on the exact phase of the laser field when the electron tunnels into the continuum, as well as the initial momentum of the electron (step 2). Most electrons do not significantly interact with the parent ion after the tunnel-ionization step, and correspond to the "direct" electrons detected in SFI. However, some electrons are driven back to the parent ion, often at very high kinetic energies (step 3). In HHG, the electron recombines with the parent ion and releases its kinetic energy in the form of a high-energy photon. In SFI, the electron can elastically scatter from the parent ion. It is these rescattered electrons that can encode the structural information of the parent atom or molecule [17] and also provide insight into the fraction of the wave packet that can undergo HHG [20,21].

In contrast to linearly polarized fields, an elliptically polarized laser field drives the electrons away from the parent ion, thereby suppressing electron-ion rescattering and HHG when the ellipticity is increased. However, rescattering and HHG may still occur for various reasons, including quantum-mechanical wave-packet spreading, the finite extent of the ionic wave function, and the nonzero initial momentum of the liberated electron. Still, for many years, the direct generation of circularly polarized beams via HHG was considered highly inefficient, if not impossible. Fortunately, theoretical schemes for generating circularly polarized HHG using counter-rotating two-color laser fields have been proposed [22–25]. As recently demonstrated experimentally, when implemented in a phase-matched geometry [26], bright, circularly polarized extreme ultraviolet [22–25,27–29] and soft-x-ray [30,31] beams are produced. These driving laser fields generate exotic waveforms that can drive electrons back to the parent ion in two-dimensional trajectories [32], separating the tunneling and rescattering angles, informing the next-generation of experiments for studying molecular dynamics on the ultrafast time scale. The influence of the Coulomb potential on laser-driven electrons in such laser fields has already been

*Corresponding author: christopher.mancuso@jila.colorado.edu

†Present address: Department of Physics and Astronomy, University of California at Irvine, Irvine, CA 92697, USA.

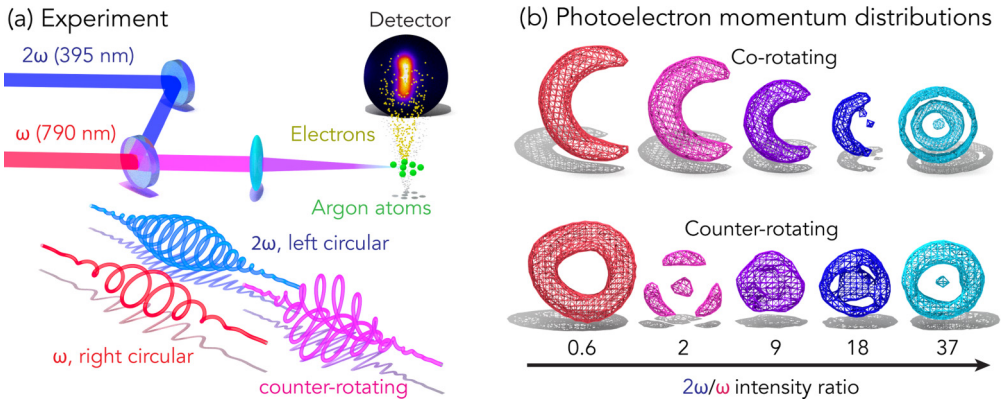

FIG. 1. (a) The experimental setup used to study strong-field ionization in two-color (ω, 2ω) circularly polarized fields. The experimental apparatus consists of a femtosecond laser system, a Mach-Zehnder interferometer, and a velocity map imaging spectrometer. (b) Experimentally measured 3D photoelectron momentum distributions at different intensity ratios for both co- and counter-rotating fields.

confirmed experimentally by observing a low-energy structure in the photoelectron distribution generated by SFI using counter-rotating fields [33].

While circularly polarized HHG is already serving as a breakthrough light source to study magnetic materials [28–31] and chiral molecules [34], there remain open questions regarding how the two fields might be optimized in order to provide brighter and higher-energy light sources. For example, it is not clear what ratio of driving laser intensities best optimizes the energy, flux, and bandwidth of the circularly polarized high-harmonic beam. Additionally, some studies have suggested that electron-ion recollision may also be possible with co-rotating fields [35–37], and indeed HHG using co-rotating fields has been reported experimentally, although with extremely low yield [22]. It is not straightforward to explore these ideas directly through HHG, since the experimentally observed harmonic spectrum and flux are typically dominated by macroscopic phase-matching effects, which although critical for applications, can conceal the single-atom physics.

In this study, we directly observe the single-atom physics of strong-field ionization of atoms in two-color counter-rotating and co-rotating laser fields by recording the photoelectron distributions that result from SFI. We gain a deep understanding of the laser-driven electron dynamics through a systematic comparison of experimental data with a comprehensive array of theoretical models, including fully-quantum-mechanical simulations using the time-dependent Schrödinger equation (TDSE), numerical simulations within the improved strong-field approximation (ISFA), intuitive calculations using the classical trajectory Monte Carlo (CTMC) method, and straightforward analytical expressions using a two-step classical trajectory (TSCT) model [38]. We find excellent agreement between our experimental results and the more sophisticated theoretical models (TDSE and ISFA). We also find qualitative agreement with the simplified models, which provide considerable physical insight into two-color circularly polarized strong-field ionization.

Additionally, in contrast to previous studies that only observed low-energy rescattered electrons [33], we observe high-energy rescattered electrons resulting from SFI driven with two-color circularly polarized fields. In agreement with our theoretical models, we find that the yield of high-energy rescattered electrons is optimized for a $I_{2\omega}/I_{\omega}$ ratio (the intensity of the second-harmonic field divided by that of the fundamental field) of $\sim$4. This finding has important implications for optimizing circularly polarized HHG. Also, we observe significantly reduced electron-ion rescattering from co-rotating fields compared to counter-rotating fields, suggesting that the single-atom HHG flux is optimized by using counter-rotating laser fields, as opposed to co-rotating fields.

II. EXPERIMENTAL SETUP

To study SFI driven by two-color circularly polarized laser fields, we used a velocity map imaging spectrometer [39] to generate two-dimensional (2D) projections of the three-dimensional (3D) photoelectron momentum distributions and recorded them using a microchannel-plate–phosphor-screen detector (Beam Imaging Solutions) imaged by a CCD camera [Fig. 1(a)]. The fundamental laser pulses (4 kHz, 790 nm, 45 fs, 3 mJ) were derived from a Ti:sapphire regenerative laser amplifier (KMLabs Wyvern HP), while the 395-nm pulses were obtained via second-harmonic generation in a 200-μm-thick β-barium borate (BBO) crystal. Dichroic mirrors were used to separate, and later recombine, the fundamental and second harmonic pulses in a Mach-Zehnder geometry. A delay stage was placed in the 395-nm arm to control the relative time delay of the laser pulses. Wave plates ($\lambda/4$ and $\lambda/2$) were placed in each beam to separately control the polarization of the 395- and 790-nm laser pulses. To control the relative intensity, a $\lambda/2$ wave plate and thin-film polarizer were placed in the 790-nm arm. Additionally, a one-to-one magnification telescope consisting of two lenses was placed in the 790-nm arm to compensate for chromatic aberration in the final focusing lens. The laser pulses were then focused into a skimmed supersonic jet of argon gas. The fundamental- and second-harmonic fields were combined in two distinct cases: with the laser fields counter-rotating (opposite helicity), and co-rotating (same helicity).

One method to understand the physics of strong-field ionization under two-color circularly polarized fields would be to directly record the photoelectron distribution in the plane of the laser polarization (xy plane). However, the plane of

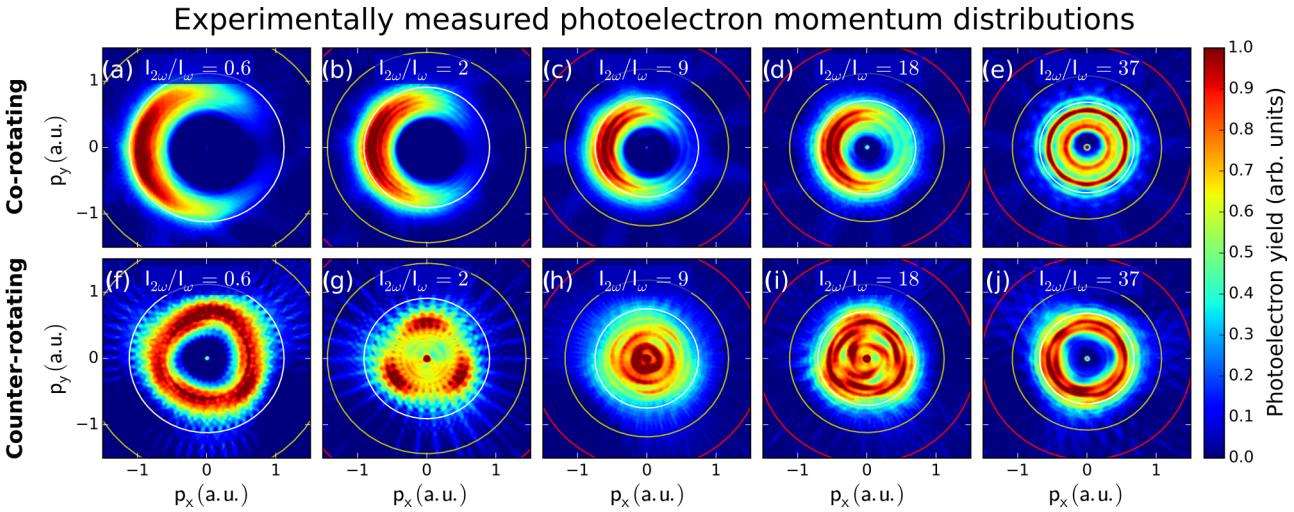

FIG. 2. Photoelectron distributions for co-rotating (a–e) and counter-rotating (f–j) fields for various intensity ratios of the 395-nm (2ω) and 790-nm (ω) driving lasers. The shape of the distributions from co-rotating fields is not highly dependent on the intensity ratio, and the electrons are driven to lower final momenta as the $I_{2\omega}/I_\omega$ ratio is increased. For the counter-rotating cases, the shape of the momentum distributions is much more sensitive to the exact intensity ratio. The white, yellow, and red rings correspond to 2, 5, and 10 U_P, respectively.

laser polarization is oriented orthogonally to the detector and information in the x direction is lost. Fortunately, the complete 3D photoelectron distribution can be recovered by applying a tomographic reconstruction algorithm [33,40] to many 2D projections recorded at different angles. Conveniently, as the relative time delay between the 395- and 790-nm fields is varied, the shape of the combined field remains fixed, but rotates around the laser-propagation axis. In the experiment, we recorded photoelectron distributions as a function of the time delay between the fundamental and second harmonic beams, using a step size of ∼133 as. The inverse Radon transform (numerically implemented using the filtered back-projection method) [41,42] was used to reconstruct the 3D distributions. The validity of the 3D photoelectron distributions obtained using the tomographic approach was confirmed by comparison with numerical solutions of the time-dependent Schrödinger equation (Appendix B).

The intensity in each beam was independently calibrated from the peak of the photoelectron momentum distribution for a one-color circularly polarized laser field, which exhibits a peak at the ponderomotive energy [43], defined as $U_P = (e^2 I)/(2c\epsilon_0 m_e \omega_0^2)$, where I is the intensity and ω_0 the frequency of the driving laser, e is the charge of the electron, c is the speed of light, m_e is the mass of the electron, and ϵ_0 is the vacuum permittivity. The total laser intensity was then held roughly constant, between $\sim 1.7 \times 10^{14}$ and $3.0 \times 10^{14}\,\mathrm{W\,cm^{-2}}$, as the $I_{2\omega}/I_\omega$ ratio was increased from ∼0.6 to 37.

III. EXPERIMENTAL RESULTS

Photoelectron momentum distributions from SFI in both co- and counter-rotating fields were measured at a number of relative intensities [Figs. 1(b) and 2]. In general, the shape and symmetry of the distributions differ substantially between the two cases. For the co-rotating case, when the field intensities are roughly comparable [Figs. 2(a)–2(c)] the photoelectron distributions consist of a single crescent-shaped lobe due to the fact that the electric field maximizes only once per 790-nm laser cycle [33]. When the second-harmonic field is much stronger [Fig. 2(e)], a torus-shaped distribution is generated that resembles SFI from a one-color circularly polarized laser. In addition, as the $I_{2\omega}/I_\omega$ ratio is increased, the U_P of the two-color field decreases, and the electrons are driven to lower final momenta. (Note that the U_P of the two-color field is simply the sum of the U_P of each field, and that the low-intensity "spikes" that extend radially from the distributions are artifacts generated in the reconstruction algorithm.)

In contrast, the photoelectron distributions in the counter-rotating case are extremely sensitive to the exact intensity ratio of the driving lasers. For counter-rotating fields with roughly equal field strengths, three ionization events occur per 790-nm laser cycle [33], which produce photoelectron distributions with threefold symmetry. When the $I_{2\omega}/I_\omega$ ratio is at its lowest [Fig. 2(f)] the distribution takes on a triangular shape and the electrons are driven to relatively high momenta. When the $I_{2\omega}/I_\omega$ ratio is increased to ∼2 [Fig. 2(g)], the familiar "three-leaf clover" distribution [33] is generated. As the $I_{2\omega}/I_\omega$ ratio is increased further to ∼9, the distribution moves to near-zero momenta [Fig. 2(h)]. As the $I_{2\omega}/I_\omega$ intensity ratio is increased to its highest values [Figs. 2(i) and 2(j)], the photoelectron distribution takes on a toroidal shape similar to that generated by a one-color circular polarized field. Interestingly, the toroidal distribution from the counter-rotating fields [Fig. 2(j)] is not identical to that from co-rotating fields [Fig. 2(e)], indicating that even a small amount of fundamental light can have a significant effect on the photoelectron momentum distribution.

In addition to measuring the photoelectron distributions corresponding to the direct electrons (relatively low energy), we experimentally observe high-energy rescattered electrons in two-color circularly polarized fields (Fig. 3). The yield of high-energy rescattered electrons is orders of magnitude lower than that of the direct electrons [44]. Consequently, the high-energy electrons are not clearly visible in the tomographic

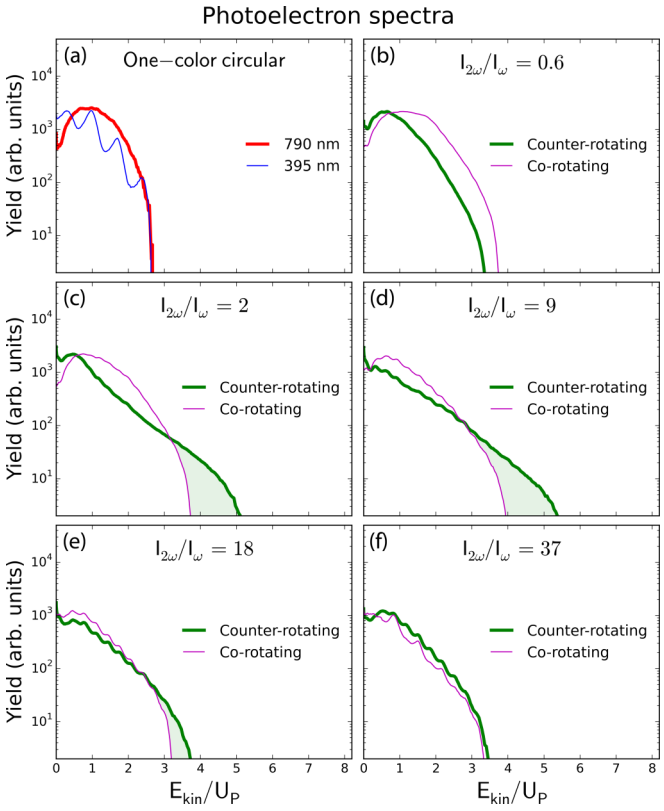

FIG. 3. (a) Photoelectron kinetic energy spectrum resulting from SFI using one-color circularly polarized fields. The peak at U_P was used to calibrate the experimental laser intensities. (b–f) Comparison of the photoelectron spectra for counter- and co-rotating fields for various intensity ratios of the 395- and 790-nm fields. For co-rotating fields, little or no high-energy electron yield is observed. For the counter-rotating cases, an enhancement of high-energy electrons (green shaded region) is observed for $I_{2\omega}/I_\omega$ ratios of ∼2, 9, and 18. The kinetic energy of the electron is expressed in units of the ponderomotive energy of the two-color field.

reconstructions (Fig. 2) since the reconstruction algorithm projects small fluctuations in the low-energy photoelectron yield as noise at high energies. Thus, to observe these high-energy electrons, we look directly at a thin slice (width ≈ 0.15 a.u. of momentum) at the center of the time-delay-averaged photoelectron distributions.

As an electron is driven by the laser field, it can re-encounter the parent ion and undergo either "soft" (low-momentum transfer) forward scattering, which produces low-energy structures [2,33,45,46], or "hard" (high-momentum transfer) backscattering, which can produce electrons at high final momenta [20]. The observation of these hard backscattered electrons is significant because they pass very close to the parent ion and have the opportunity to record information about the atomic or molecular structure [17,18,47–50]. Also, the trajectories associated with these hard backscattered electrons are nearly identical to the trajectories that recombine to produce HHG. Thus, understanding the conditions that optimize the high-energy electron yield informs how to optimize the single-atom yield of HHG [20,21].

We find that counter-rotating fields provide significantly more high-energy electrons than co-rotating fields in situations where the $I_{2\omega}/I_\omega$ ratio is between ∼2 and 9 [Figs. 3(c) and 3(d)]. This also corresponds to the approximate range where calculations (Sec. IV) suggest that electron-ion rescattering should occur in counter-rotating fields. When the $I_{2\omega}/I_\omega$ ratio is very low [Fig. 3(b)] or very high [Fig. 3(f)], the photoelectron distributions for the co- and counter-rotating cases are very similar and exhibit a maximum in yield followed by a sharp dropoff. For $I_{2\omega}/I_\omega$ ratios between ∼2 and 9 [Figs. 3(c) and 3(d)], the photoelectron distributions from the counter-rotating fields exhibit a "plateau" that extends the electrons to higher energies, in direct analogy to a similar rescattering-induced plateau observed in SFI [44] and HHG driven by linearly polarized fields [3]. This behavior cannot be explained in terms of the direct electrons (Sec. IV A), but can be attributed to hard electron-ion rescattering [44,51].

IV. DISCUSSION

A. Two-step classical trajectory model

The basic shape and symmetry of the direct photoelectron distribution can be estimated using the TSCT model. In TSCT, the first step is to simulate ionization by setting an electron free at different times (t_b) over one-cycle of the two-color circularly polarized laser field. The probability that an electron is ionized is given by the ADK rate [52], which depends nonlinearly on the electric field strength at t_b. In the second step, the ionized electron is placed at the center of the parent ion, and the electron trajectory is calculated using a classical equation of motion, where all effects of the Coulomb potential are ignored. The electric field of the two-color circularly polarized laser is given by

$$\begin{aligned}\vec{E}(t) = &\frac{E_{0,R}}{\left(1+\xi_R^2\right)^{1/2}}[\cos(\omega_R t-\phi_R)\hat{x}+\xi_R\sin(\omega_R t-\phi_R)\hat{y}]\\ &+\frac{E_{0,B}}{\left(1+\xi_B^2\right)^{1/2}}[\cos(\omega_B t-\phi_B)\hat{x}\\ &\pm\xi_B\sin(\omega_B t-\phi_B)\hat{y}],\end{aligned} \tag{1}$$

where t is time, ω is the frequency, ϕ is the phase delay, E_0 is the maximum amplitude of the electric field, ξ is the ellipticity, $\hat{x}$ and $\hat{y}$ are orthogonal unit vectors, the subscripts R and B denote the 790-nm ("red") and 395-nm ("blue") beams, and the positive (negative) sign in the last line specifies co-rotating (counter-rotating) fields. The electron momentum is given by

$$\vec{p}(t_b) = e[\vec{A}(t_b)-\vec{A}(t)] = e\int_{t_b}^{t}\vec{E}(t')dt', \tag{2}$$

where t_b is the time the electron is ionized, and $\vec{A}(t)$ is the vector potential of the laser. The final drift momentum of the electron is obtained by retaining terms that do not oscillate in time. This approximation is valid when the electron does not leave the focal volume during the laser pulse [53], a condition satisfied by the experimental conditions used in this study.

The major differences between the photoelectron distributions from co- and counter-rotating fields can be explained by considering the relationship between the electric field and the final drift momentum (Fig. 4). Since the ionization rate is highly nonlinear with the electric field [52], the photoelectron distribution will be dominated by electrons that tunnel near the peak of the electric field. In the case of co-rotating fields,

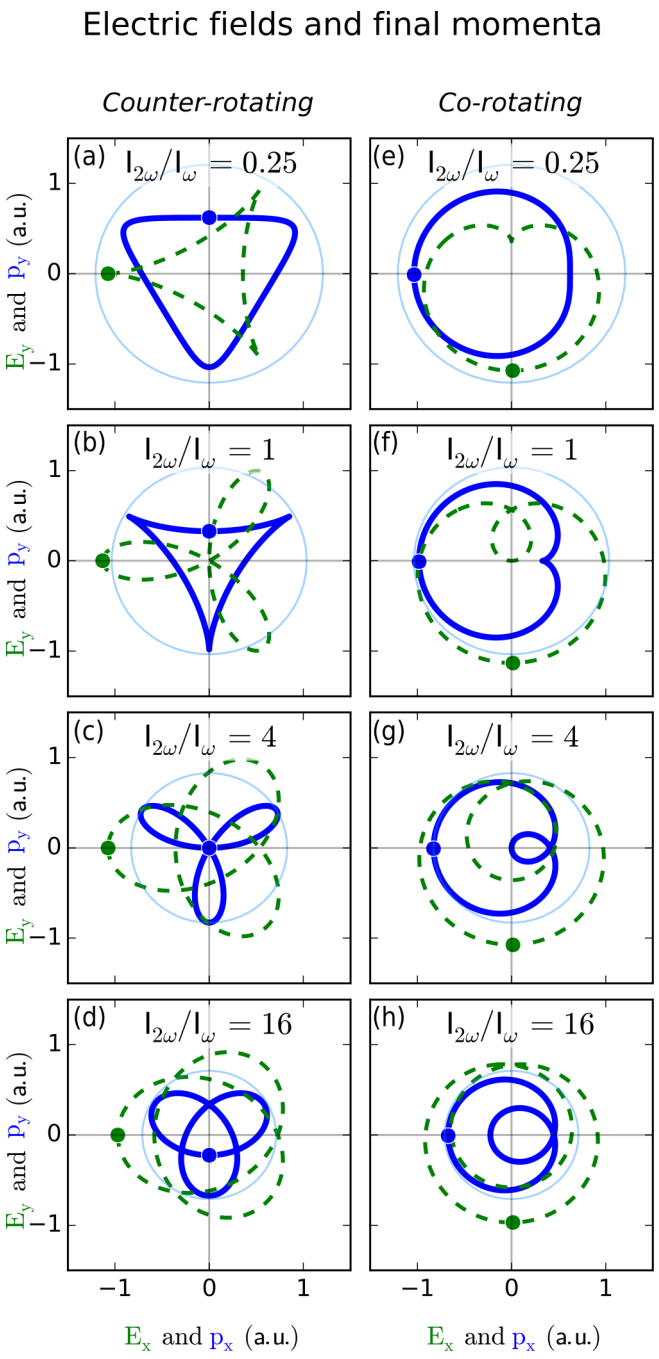

FIG. 4. Electric fields (green dashed line) and final electron drift momenta (blue solid line). The dots represent time zero for each field and demonstrate that for counter-rotating fields, a maximum of the electric field corresponds to a minimum in the drift momentum. Conversely, for co-rotating fields, a maximum in the electric field corresponds to a maximum of the final drift momentum. The total intensity of each ratio is 2×10^{14} W cm^{-2}, and the light-blue circle indicates a final drift momentum of $2\,U_P$. The electric field is scaled in order to be displayed on the same axes as the final drift momentum.

the peak of the electric field corresponds to the maximum of the final drift momentum. For counter-rotating fields, each peak of the field corresponds to a minimum of the final drift momentum. Thus, in the absence of electron-ion rescattering, co-rotating fields produce (on average) photoelectrons with higher energies than counter-rotating fields.

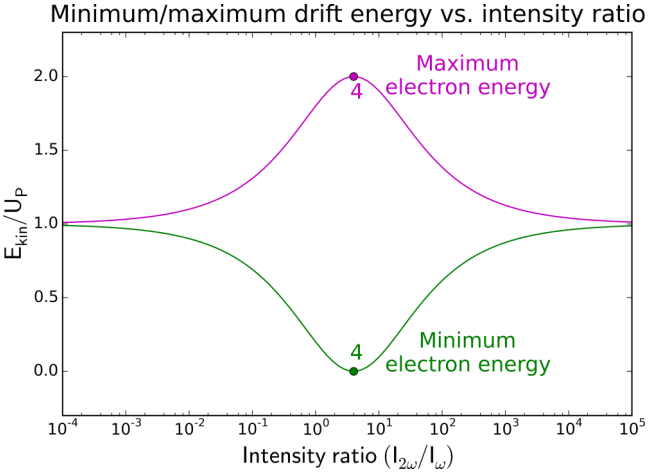

FIG. 5. Cutoff energies of the direct electrons for different intensity ratios. The largest separation of the minimum and maximum energies occurs when the $I_{2\omega}/I_\omega$ ratio is 4 (circles). These curves apply to both co- and counter-rotating fields. However, photoelectron distributions for counter-rotating fields have the greatest yield at the minimum electron energy (green), while photoelectron distributions for co-rotating fields have the greatest yield at the maximum electron energy (magenta).

As the $I_{2\omega}/I_\omega$ ratio is varied, the minimum and maximum energy of the direct electrons changes (Fig. 5). In the limiting cases, where the $I_{2\omega}/I_\omega$ ratio approaches zero or infinity, the minimum and maximum electron energies both converge to U_P, which is well known for one-color, circularly polarized fields [43]. As the $I_{2\omega}/I_\omega$ ratio is varied, the minimum and maximum electron energies split and have a greatest separation for a $I_{2\omega}/I_\omega$ ratio of 4, which corresponds to the U_P of each field being equal. Here the minimum and maximum energies reach values of 0 and 2 U_P respectively, which resembles the case for one-color, linearly polarized fields [43]. While both co- and counter-rotating fields have the same minimum and maximum electron energy, the different relationship between $\vec{E}(t)$ and $\vec{p}(t)$ in the two cases (Fig. 4) means that counter-rotating fields will produce a distribution that is peaked at the *minimum* electron energy, while co-rotating fields will produce a distribution that is peaked at the *maximum* electron energy.

The 2D photoelectron distributions can be estimated in the TSCT (Fig. 6) by weighting the final drift momenta by the tunnel-ionization rate, which depends nonlinearly upon the strength of the electric field [52]. As expected from Fig. 5, counter-rotating fields drive a majority of electrons to low final energies when the fields are roughly equal, while co-rotating fields drive most electrons to higher energies. The photoelectron distributions from the TSCT (Fig. 6) agree well with the experimental data (Fig. 2). The shape of the distributions from co-rotating fields is not highly dependent on the intensity ratio, but for counter-rotating fields, several qualitatively different shapes are observed as the intensity ratio is varied. For example, when the $I_{2\omega}/I_\omega$ ratio is roughly equal [Figs. 6(a) and 6(b)], three distinct ionization events can be seen. When the $I_{2\omega}/I_\omega$ ratio is increased to 4 [Fig. 6(c)], the electrons are driven to a minimum in the momentum spectrum.

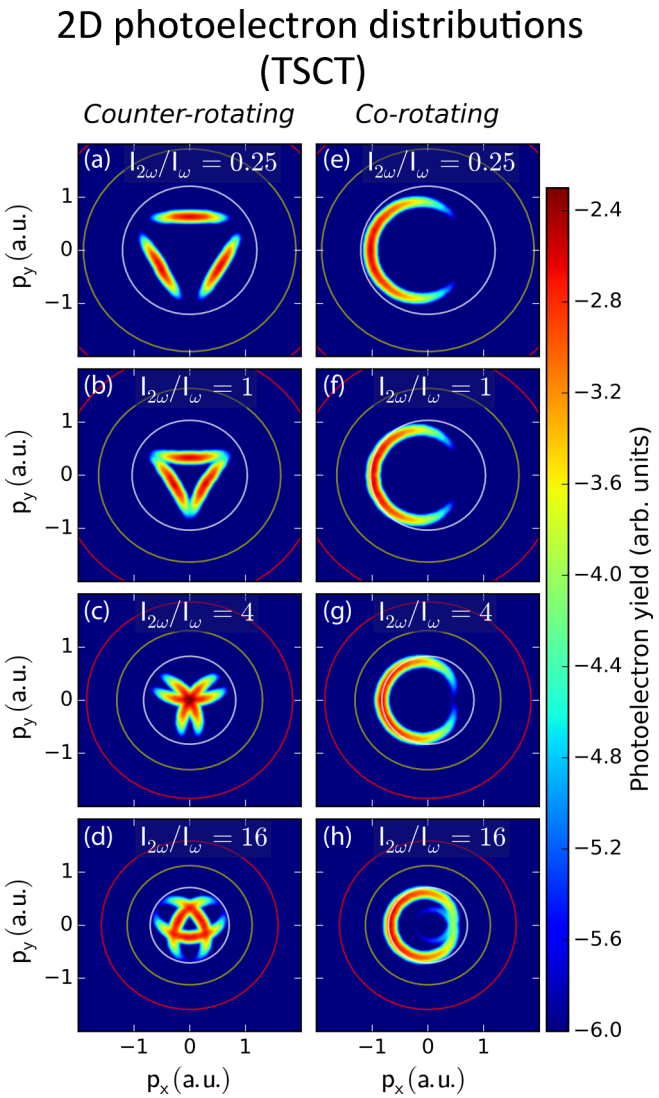

FIG. 6. Photoelectron distributions of the direct electrons calculated using the two-step classical trajectory (TSCT) plotted on a log scale. The distributions are obtained by weighting the classically derived final drift momenta by the tunnel-ionization rates. The effect of the Coulomb potential is ignored and a Gaussian distribution of initial momenta is assumed. The total intensity for each ratio is 2×10^{14} W cm^{-2}, and the white, yellow, and red rings correspond to 2, 5, and 10 U_P, respectively.

As the $I_{2\omega}/I_\omega$ ratio is increased further to 16 [Fig. 6(d)], electrons are again driven to higher momenta.

To gain an intuitive understanding of how we can control the rescattering process by changing the relative intensity ratio, we analyzed the electron trajectories within the TSCT and identified the likelihood for electrons to pass in close proximity to the parent ion (Fig. 7). In the TSCT, the electron trajectories are entirely determined by the electric field of the laser, and the position and velocity of an electron can be determined by simply integrating $\vec{a} = (e/m_e)\vec{E}(t)$, where $\vec{a}$ is the electron's acceleration, and $\vec{E}(t)$ is the electric field of the two-color laser field [Eq. (1)] as a function of time. To estimate the probability of rescattering, electron trajectories were calculated for a number of different ionization times. If an electron then passed

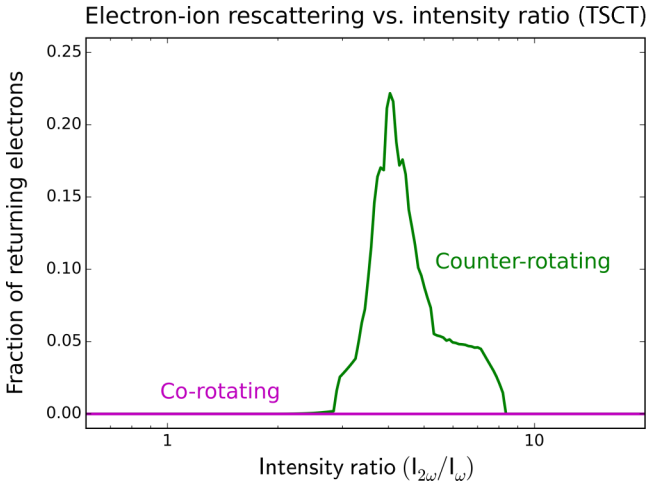

FIG. 7. The fraction of electrons that pass within 0.05 nm of the parent ion provides an estimate of the probability for hard electron-ion rescattering and HHG. In the TSCT, this type of electron-ion rescattering is optimized at a $I_{2\omega}/I_\omega$ ratio of 4 for counter-rotating fields (green), while for co-rotating fields (magenta), no electrons are driven back in close proximity of the parent ion.

within 0.05 nm (about 1 Bohr radius) of the parent ion, the electron was considered rescattered, and the probability of this trajectory was weighted by the tunnel-ionization rate. This method for estimating the probability of hard electron-ion rescattering does not take into account effects such as the quantum-mechanical rescattering probability, which decreases the likelihood of hard rescattering by orders of magnitude. Nonetheless, this metric should predict at which intensity ratios hard rescattering (and HHG) is optimized.

For the counter-rotating case (Fig. 7, green curve), the probability of electrons being driven back in close proximity of the parent ion depends strongly on the intensity ratio. The number of close-proximity electrons reaches a maximum around a $I_{2\omega}/I_\omega$ ratio of 4, and the window where electrons pass within 0.05 nm of the ion spans from a $I_{2\omega}/I_\omega$ ratio of $\sim$2 to $\sim$9. This agrees very well with the experimental data (Fig. 3). More generally, the rescattering process optimizes when the ponderomotive energy for each individual driving laser field is the same, regardless of the frequencies of the two-color field (Appendix D). For the co-rotating case (Fig. 7, magenta curve), no electrons are driven back within 0.05 nm of the parent ion, which suggests that high-energy rescattering should be completely suppressed. However, this simple model ignores the Coulomb field and does not include initial momenta of the electron. Including these effects would increase the likelihood of electron-ion rescattering and broaden the range of relative intensities that could result in electron-ion rescattering. However, we expect the general conclusions of the TSCT to remain valid: counter-rotating fields return electrons to the ion much more effectively than co-rotating fields, and a $I_{2\omega}/I_\omega$ ratio of $\sim$4 should optimize the probability of electron-ion rescattering.

B. Numerical improved strong-field approximation (ISFA) calculations

While the TSCT provides qualitative understanding of electron dynamics in two-color circularly polarized fields, more

sophisticated simulations can provide quantitative insight. An effective tool for providing such quantitative descriptions of atoms in strong laser fields is the improved strong-field approximation (ISFA) [43,54]. Previously, the ISFA has been successfully applied to study high-order channel closing effects [54,55], low-energy structures in above-threshold ionization with linearly polarized fields [56], above-threshold detachment in two-color circularly polarized fields [55,57], and laser-assisted recombination [58]. In the ISFA, the exact S-matrix is expanded in a Born series in the rescattering potential, where the zero-order term corresponds to the direct-electron spectra, and the first-order term to the rescattered-electron spectra. A realistic wave function of argon (Eq. (20) in Ref. [54]) and electron-ion rescattering potential (Eq. (21) in Ref. [54]) were used to compute the transition amplitudes. The effect of the Coulomb potential on the outbound electron enters via the first-order expansion term. The ISFA photoelectron spectrum is calculated as a double integral over time (Eqs. (13)–(19) in Ref. [54]), with an infinitely long laser pulse at an intensity of 2×10^{14} W cm^{-2}.

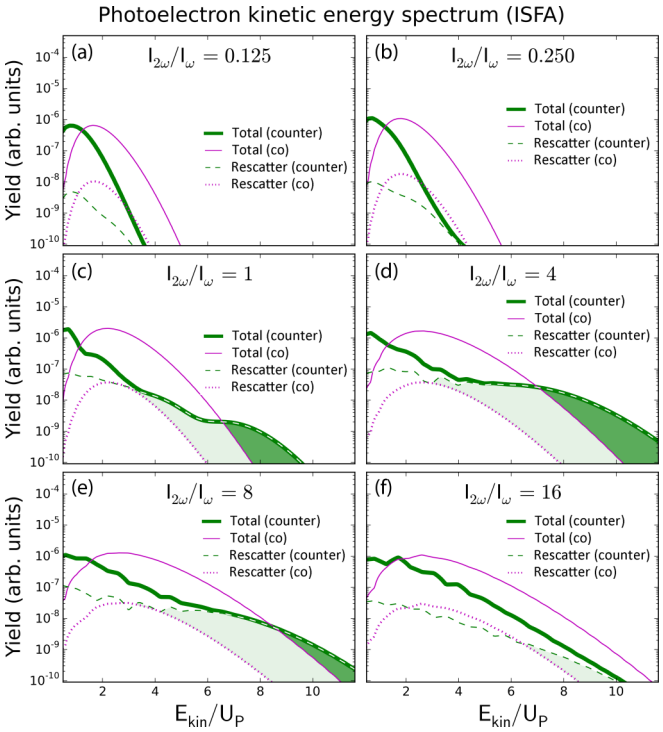

FIG. 8. Photoelectron distributions obtained from the direct and rescattering terms of the ISFA simulations. The total (direct+rescattering, solid lines) term of the ISFA agrees well with the experimental data (Fig. 3), showing an enhancement of high-energy electrons (dark green region) that result from hard electron-ion backscattering and are seen in the counter-rotating case when the $I_{2\omega}/I_\omega$ ratio is 1, 4, and 8 with a maximum at 4. The rescattering term (dashed and dotted lines) of the ISFA shows an even greater enhancement (light and dark green shaded regions) of the hard rescattered electrons. This effect is masked in the experimental spectra as co-rotating cases can drive the more populous direct and soft rescattered electron to fairly high energies. The total intensity for each ratio is 2×10^{14} W cm^{-2}, and the kinetic energy of the electron is expressed in units of the ponderomotive energy of the two-color field.

The photoelectron distributions obtained via the ISFA numerical simulations are presented for two cases (Fig. 8); the total photoelectron distributions consisting of the direct and rescattering electrons, and the distributions solely composed of rescattered electrons. For cases when the $I_{2\omega}/I_\omega$ ratio is less than 1 [Figs. 8(a) and 8(b)], the total photoelectron spectra consist mostly of direct electrons, and therefore can be described adequately by the TSCT. As the $I_{2\omega}/I_\omega$ ratio is increased to values of 1, 4, and 8 [Figs. 8(c)–8(e)], the shape of the co-rotating electron spectra does not change significantly from the lower-ratio cases. However, for the counter-rotating cases, a plateau begins to form, indicative of backscattering [44]. As the $I_{2\omega}/I_\omega$ ratio is increased beyond 8 [Fig. 8(f)], the electron spectra for the counter-rotating cases lose the plateau structure, signaling that backscattering is again suppressed. For the co-rotating cases, the total and rescattering terms are identical in shape, but simply differ by a constant factor for all $I_{2\omega}/I_\omega$ ratios, indicating backscattering does not play an important role.

The dark green shaded region in Fig. 8 highlights the difference between the total photoelectron yield for the co- and counter-rotating cases, and agrees well with the experimental data (Fig. 3). Additionally, the difference in just the rescattered electron contribution between the co- and counter-rotating cases is highlighted in Fig. 8 by both the light and dark green shaded regions. The difference in the rescattering term confirms that the high-energy plateau is indeed dominated by rescattered electrons, and that the window over which hard backscattering occurs ranges from $I_{2\omega}/I_\omega$ ratios of approximately 1–8 and is optimized at a ratio of 4.

One striking feature of the photoelectrons' distributions is the broadening of the spectral width as the $I_{2\omega}/I_\omega$ ratio is increased. This trend is explained by Delone and Krainov [59]. In this paper, the photoelectron distribution as a function of the electron's final drift energy is calculated for ionization by a one-color circularly polarized laser field, where no rescattering takes place. This equation (Eq. (33) in Ref. [59]) can be recast into a form more relevant to this manuscript:

$$w(E/U_P) = w_{\max} \exp\left[-\left(\frac{\sqrt{I_P \frac{I}{2}}}{2\omega^2}\right)\left(\frac{E}{U_P} - 1\right)^2\right], \quad (3)$$

where w is the ionization rate, $w_{\max}$ is the maximum of the rate, which depends on the laser intensity, E is the final drift energy of the electron, I_P is the ionization energy of the atom, and I and ω are the intensity of the frequency of the driving laser field, respectively. In the simulations I_P and I are held constant, so the width of the photoelectron spectrum, as given in terms of E/U_P, solely depends on ω. In the limits where one or the other frequency is dominant, this formula agrees well with the ISFA simulations, showing that as the $I_{2\omega}/I_\omega$ is increased, which in effect increases the total frequency of the two-color field, the photoelectron distributions become broader. One slight difference is that in Eq. (3) the maximum in a one-color circularly polarized field is always at U_P; however, in a two-color circularly polarized field this maximum changes depending on the $I_{2\omega}/I_\omega$ ratio, as described in Fig. 5.

C. Classical trajectory Monte Carlo simulations

The effect of electron-ion rescattering in two-color circularly polarized fields was further studied in a semiclassical context by carrying out classical trajectory Monte Carlo (CTMC) numerical simulations. In these simulations, electrons are placed into the continuum at an appropriate tunneling distance with their tunneling time and initial momentum given by random sampling. In the CTMC simulations, the two-color field was given by Eq. (1), but with an additional pulse envelope with a full width at half maximum (FWHM) of 20 fs. Ionization was restricted to ± 2.67 fs near the peak of the pulse (corresponding to two cycles of the 790-nm field), and the probability of ionization was weighted by the tunnel-ionization rates [52]. The longitudinal and transverse initial momenta were randomly sampled from a Gaussian distribution centered at zero momentum with a standard deviation of 0.25 a.u. of momentum. For further details, see Appendix A.

In similar fashion to the ISFA simulations, the CTMC results are shown for two cases (Fig. 9); the total photoelectron yield (solid lines), and for only those electrons considered rescattered (dashed and dotted lines). In the CTMC approach, an electron is considered rescattered if it returns within 0.05 nm of the parent ion. The CTMC results agree well with both the experimental results (Fig. 3), and the ISFA simulations (Fig. 8), in that an enhancement of a high-energy electron occurs when the $I_{2\omega}/I_{\omega}$ ratio is between 1 and 8, and optimizes at a ratio of 4 (shaded green regions).

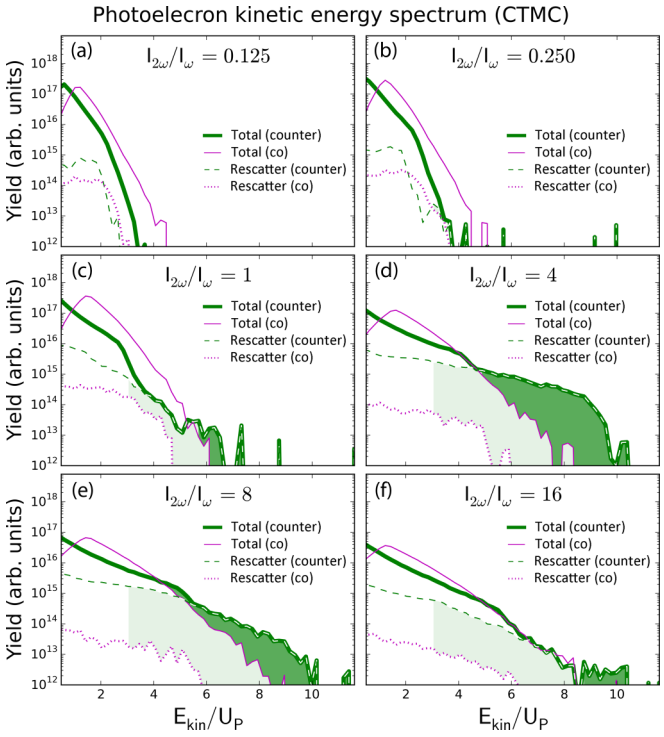

FIG. 9. Photoelectron distributions obtained from CTMC simulations. The total photoelectron yield (solid lines) agrees well with the experimental data (Fig. 3), showing an enhancement of high-energy electrons (dark green region) that result from hard electron-ion backscattering and are seen in the counter-rotating case when the $I_{2\omega}/I_{\omega}$ ratio is 1, 4, and 8 with a maximum at 4. The photoelectron yield composed of only hard rescattered electrons (dashed and dotted lines), where an electron is considered rescattered if it passes within 0.05 nm of the parent ion, shows an even greater enhancement (light and dark green shaded regions) of the hard rescattered electrons, agreeing with the ISFA simulations (Fig. 8). The total intensity for each ratio is 2×10^{14} W cm^{-2}, and the kinetic energy of the electron is expressed in units of the ponderomotive energy of the two-color field.

Although the CTMC and TSCT simulations are both classical in nature, the CTMC simulations offer a more accurate description of rescattering in both co- and counter-rotating fields for two reasons. First, the CTMC simulations include the Coulomb potential, which serves to attract electrons that would otherwise not return to the parent ion. Second, the CTMC simulations incorporate a nonzero initial momentum of the electron, which enables a much larger variety of electron trajectories than the TSCT, which assumes an initial momentum of zero. Additionally, when one or the other frequency is dominant, the spectral width of the photoelectron distributions agrees with the width predicted by Delone and Krainov [59] (see Sec. IV B).

V. CONCLUSION

We investigated strong-field ionization in two-color circularly polarized fields as a function of the relative intensity of the 790- and 395-nm driving fields. We experimentally recorded three-dimensional photoelectron distributions across a broad range of intensity ratios and showed that the intricate shapes of these distributions can be described using a simple analytical model. Additionally, we experimentally observed high-energy rescattered electrons in these fields, and found the conditions that optimized electron-ion rescattering. Advanced numerical simulations confirm our experimental results, and refine the parameters that optimize rescattering and the single-atom yield in high-harmonic generation. Specifically, we found that the window of $I_{2\omega}/I_{\omega}$ ratios under which significant rescattering occurs is fairly broad, and is optimized near a ratio of 4. In general, the rescattering process optimizes when the ponderomotive energy for each field is equal, regardless of the frequencies of the two-color field. In addition, both the experimental data and numerical simulations show that rescattering in co-rotating fields is highly suppressed compared to counter-rotating fields.

ACKNOWLEDGMENTS

The experimental work was done at JILA with funding from the U.S. Department of Energy Office of Basic Energy Sciences Atomic Molecular and Optical Sciences program. JILA also gratefully acknowledges support from an AFOSR DURIP award for the laser system used for this work. C.A.M. and J.L.E. acknowledge support from National Science Foundation Graduate Research Fellowships under Grant No. DGE 1144083. E.H. and D.B.M. gratefully acknowledge support by the Federal Ministry of Education and Science, Bosnia and Herzegovina. P.G. acknowledges support from the Deutsche Forschungsgemeinschaft (Grant No. GR 4234/1-1). X.M.T. was supported by Grant-in-Aid for Scientific Research Grant No. C24540421 from the Japan Society for the Promotion of

Science and HA-PACS Project for advanced interdisciplinary computational sciences by exascale computing technology.

APPENDIX A: CLASSICAL TRAJECTORY MONTE CARLO SIMULATIONS

Two-dimensional photoelectron momentum distributions were calculated with the CTMC method for both counter-rotating (Fig. 10) and co-rotating (Fig. 11) fields for a number of different intensity ratios. To better understand the rescattering process, the photoelectron distributions were calculated in two ways: with the Coulomb potential included, and without the Coulomb potential included. The general shapes of the distributions from the CTMC simulations (Figs. 10 and 11) agree nicely with the experimentally measured 2D photoelectron distributions (Fig. 2). There are several major differences between the distributions calculated with the Coulomb potential and those calculated without. First, low-energy structures appear, particularly for high $I_{2\omega}/I_{\omega}$ ratios. These low-energy structures result from soft-electron-ion rescattering as observed in Ref. [33]. Second, high-energy structures resulting from hard electron-ion backscattering are seen for counter-rotating cases when the $I_{2\omega}/I_{\omega}$ ratio is 4 or

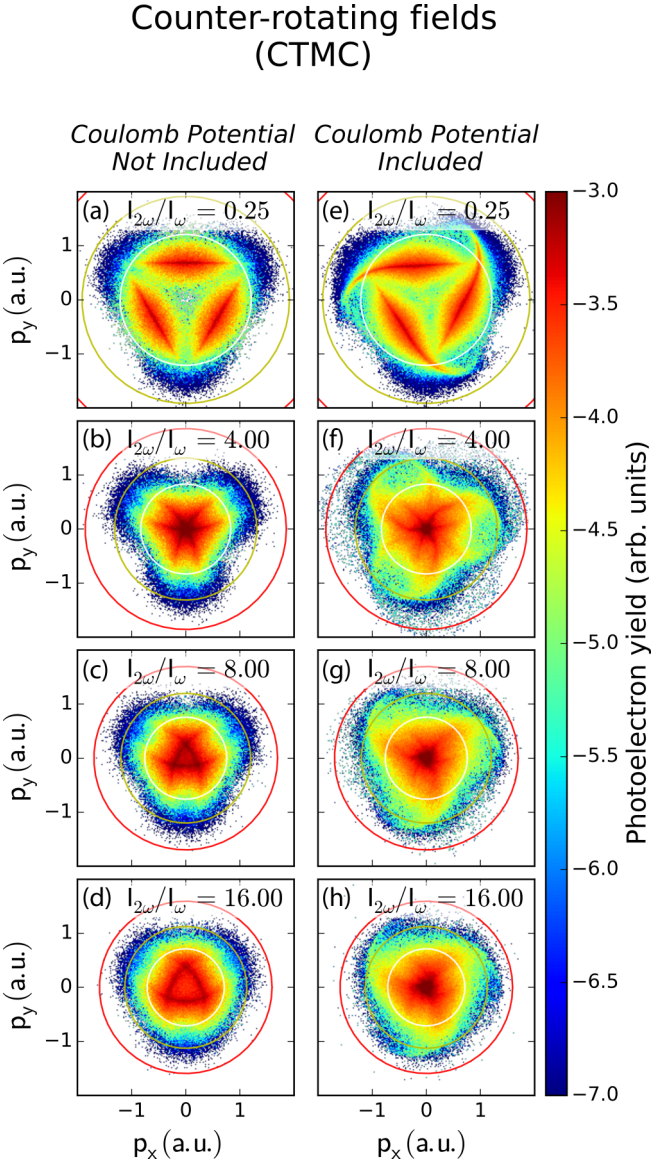

FIG. 10. Photoelectron distributions from CTMC simulations for counter-rotating fields, for when the Coulomb potential of the parent ion is not included (a–d) and included (e–h), plotted on a log scale. High-energy rescattered electrons are prominent when the $I_{2\omega}/I_{\omega}$ ratio is 4 and 8 (f,g). Additionally, there is a noticeable rotation of the distributions when the Coulomb potential is included, demonstrating the effect of the parent ion on the electron trajectories. The total intensity for each ratio is $2 \times 10^{14}\,\mathrm{W\,cm^{-2}}$, and the white, yellow, and red rings correspond to 2, 5, and 10 U_P, respectively.

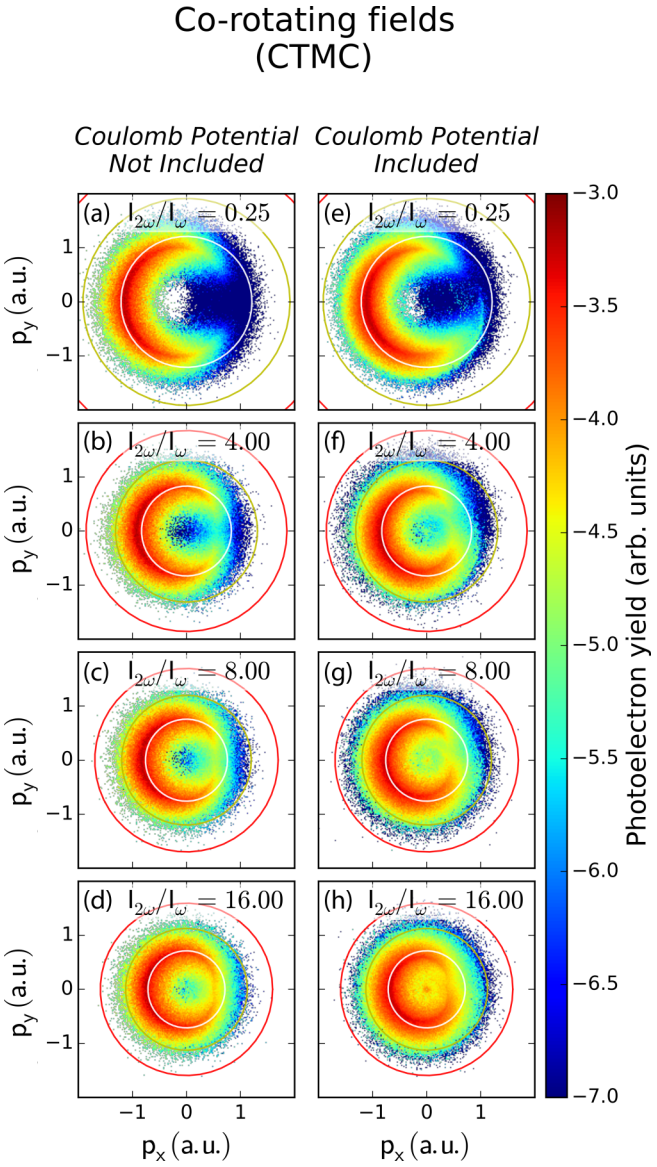

FIG. 11. Photoelectron distributions from CTMC simulations for co-rotating fields, for when the Coulomb potential of the parent ion is not included (a–d) and included (e–h), plotted on a log scale. In comparison to the counter-rotating case (Fig. 10), there is still a rotation of the distributions due to the effect of the Coulomb potential on the electron trajectories; however, there is no significant enhancement of high-energy electrons for any intensity ratio. The total intensity for each ratio is $2 \times 10^{14}\,\mathrm{W\,cm^{-2}}$, and the white, yellow, and red rings correspond to 2, 5, and 10 U_P, respectively.

8 [Figs. 10(f) and 10(g)]. There is no significant enhancement of the high-energy electrons for any of the co-rotating cases.

Finally, the CTMC simulations reveal a slight twist of the photoelectron distributions when the Coulomb potential is introduced. This effect can be seen clearly by comparing the lobes in Fig. 10(a) with those in Fig. 10(e), which appear to have been stretched in a counterclockwise fashion. Interestingly, while a counterclockwise twist is seen for all $I_{2\omega}/I_{\omega}$ ratios in the co-rotating case (Fig. 11)—where both fields rotate counterclockwise—both helicities of twist can be seen in the counter-rotating cases. Specifically, when the ω field (which rotates counterclockwise) is high, the photoelectron distribution is twisted in the counterclockwise direction. However, when the 2ω field (which rotates in the clockwise direction) is high, the distributions twist in the clockwise direction [cf. Figs. 10(c) and 10(g)].

This twist in the photoelectron distribution is due to the Coulomb potential's effect on the electron trajectories. Interestingly, the twist is not completely symmetric and, in particular for counter-rotating fields, the threefold reflection symmetry predicted by the TSCT model (Fig. 6) is lost when the electron strongly interacts with the Coulomb potential. The effect can also be seen in the experimental data (Fig. 2), and the theoretical models that include electron-ion interactions (Figs. 12 and 13).

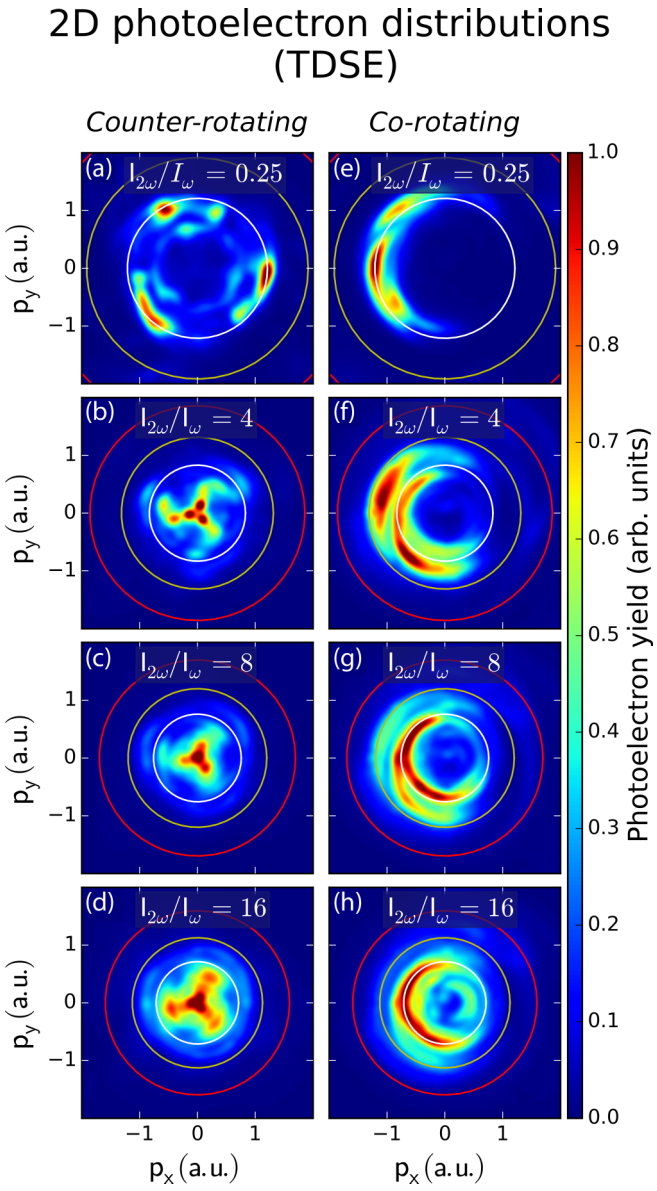

FIG. 12. 2D photoelectron distributions numerically calculated by solving the 3D time-dependent Schrödinger equation (TDSE). The numerical results are in good agreement with the experimentally measured distributions (Fig. 2). The total intensity for each ratio is $2 \times 10^{14}\,\mathrm{W\,cm^{-2}}$.

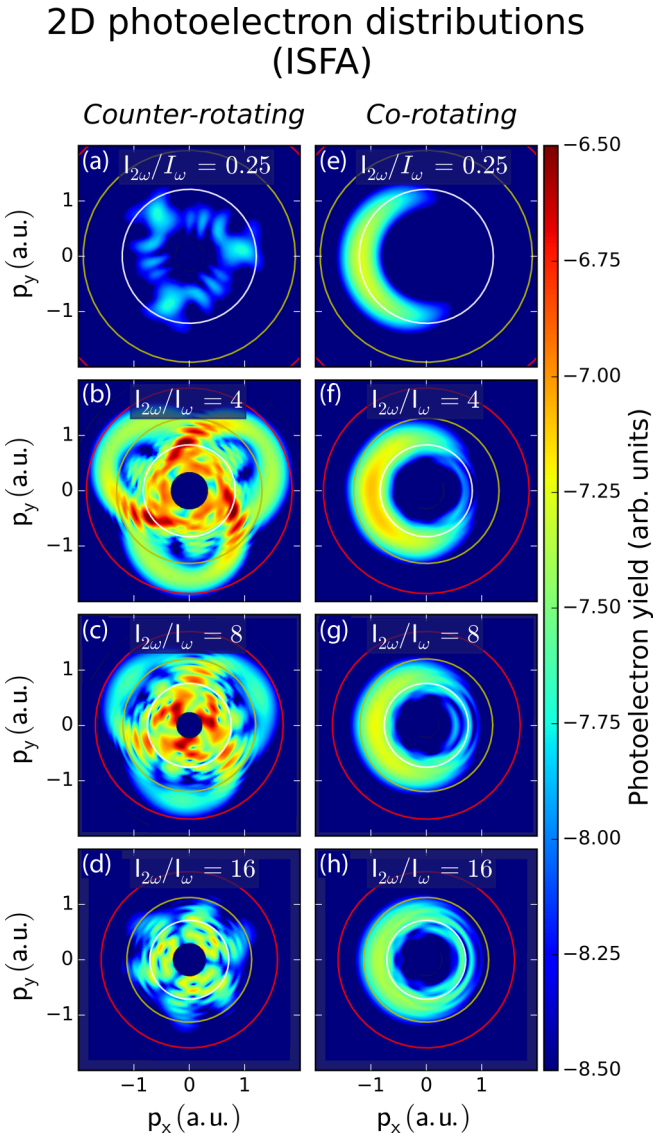

FIG. 13. 2D photoelectron momentum distributions numerically simulated using the rescattering term of the ISFA simulations for different intensity ratios plotted on a log scale. The ISFA shows significant high-energy rescattering for counter-rotating fields when the $I_{2\omega}/I_{\omega}$ ratio is 4 and 8 (b and c, respectively). The "hole" in the center of the distributions is a result of the energy conserving condition (Eq. (12) of Ref. [54]) that must be satisfied in the ISFA simulations. The total intensity for each ratio is $2 \times 10^{14}\,\mathrm{W\,cm^{-2}}$, and the white, yellow, and red rings correspond to 2, 5, and 10 U_P, respectively.

Additional details of the implementation of the CTMC method include that for each set of initial conditions, the differential equations of motion for the electron were solved using the Livermore Solver for Ordinary Differential Equations with automatic switching between stiff and nonstiff problems (LSODE) [60] as implemented in ODEPACK [61] and incorporated in SCIPY [62]. In general, trajectories that do not pass near the parent ion are considered by the integrator to be nonstiff and are integrated using a traditional multistep method (Adams-Moulton), while trajectories that pass close to the parent ion are treated with a method optimized for stiff differential equations (backward differentiation formula). This automatic switching method provides computational efficiency while maintaining the accuracy of the solution even for electrons that undergo a substantial velocity change while in close proximity to the parent ion. The initial step size was 10^{-20} s, the maximum step size was 5×10^{-18} s, and the electron trajectories were simulated for 200 fs. For each simulation, 10^6 electron trajectories were flown, requiring ~50 CPU hours per simulation.

APPENDIX B: 2D PHOTOELECTRON DISTRIBUTIONS FROM TDSE SIMULATIONS

To validate the tomographic reconstruction method to generate the experimental 3D photoelectron distributions, we solved the 3D time-dependent Schrödinger equation (TDSE) using a generalized pseudospectral method [63,64]. A Gaussian filter with $\sigma = 0.065$ a.u. of momentum was applied to the numerical results to simulate intensity averaging and allow the broad features to be seen more clearly. The photoelectron distributions from the TDSE simulations (Fig. 12) are in good agreement with the experimental data (Fig. 2). As predicted by the TSCT, the shape and energies of the distributions are highly dependent on the intensity ratio for the counter-rotating case [Figs. 12(a)–12(d)], but not for the co-rotating case [Figs. 12(e)–12(h)]. Note that the TDSE simulations are only used to model the direct (lower-energy) electrons seen experimentally in Fig. 2. Although these simulations have been used to successfully predict low-energy rescattered structures in two-color circularly polarized fields [33], they are complex numerical simulations, and have not been optimized to accurately model the high-energy rescattered electrons.

APPENDIX C: 2D PHOTOELECTRON DISTRIBUTIONS FROM ISFA SIMULATIONS

Although the integrated yields of the ISFA simulations (Fig. 8) highlight the agreement with the experimentally recorded data (Fig. 3), the 2D photoelectron distributions obtained from the ISFA simulations reveal additional information about the hard electron-ion rescattering process. High-energy structures corresponding to hard electron-ion backscattering can be seen in the counter-rotating case for $I_{2\omega}/I_\omega$ ratios of 4 and 8 [Figs. 13(b) and 13(c)]. In both cases, the high-energy rescattered electrons resemble three offset rings. These structures indicate that there are three major electron-ion rescattering events per laser cycle. The center of each ring is displaced from zero momentum by the vector potential at the time of rescattering, and the radius of each ring indicates the electron momentum at the time of rescattering. In addition, the ISFA simulations include electron interference effects, and consequently show much more structure in the electron distributions than the TSCT or the CTMC simulations, which ignore such effects.

The basic shape of the rescattering term of the ISFA (Fig. 13) agrees with that of the 2D experimental photoelectron distributions (Fig. 2). The rescattering term also reproduces the direct electron contribution because, in the ISFA, even electrons that interact very weakly with the parent ion are considered rescattered electrons.

APPENDIX D: OPTIMIZING ELECTRON-ION RESCATTERING FOR OTHER DRIVING WAVELENGTHS

To generalize the concept of how the yield of backscattered electrons depends on the intensity ratio of the two-color counter-rotating field, the TSCT was used to calculate electron trajectories that passed within 0.05 nm of the parent ion (Sec. IV A) for different combinations of driving laser wavelengths. Three cases are shown in Fig. 14: 790 nm+263 nm (ω,3ω), 790 nm+395 nm (ω,2ω), and the noncommensurate ratio of 1300 nm+790 nm (ω,1.64ω). The noncommensurate case is important as these wavelengths were used to generate bright circular soft-x-ray high-order harmonics that were used to perform the first tabletop x-ray magnetic circular dichroism measurement at the gadolinium N edge [30].

In each of the cases hard electron-ion rescattering should be optimized when the U_P of each field is the same. In general if the two-color field is composed of driving lasers at frequencies ω and $n\omega$, the optimum $I_{n\omega}/I_\omega$ ratio is n^2, as $U_P \propto 1/\omega^2$. This can be seen in Fig. 14 where the 790 nm+263 nm case optimizes at ~9, the 790 nm+395 nm case optimizes at ~4, and the 1300 nm+790 nm case optimizes at ~2.7. This can be extended to the case for a (ω,ω) counter-rotating field,

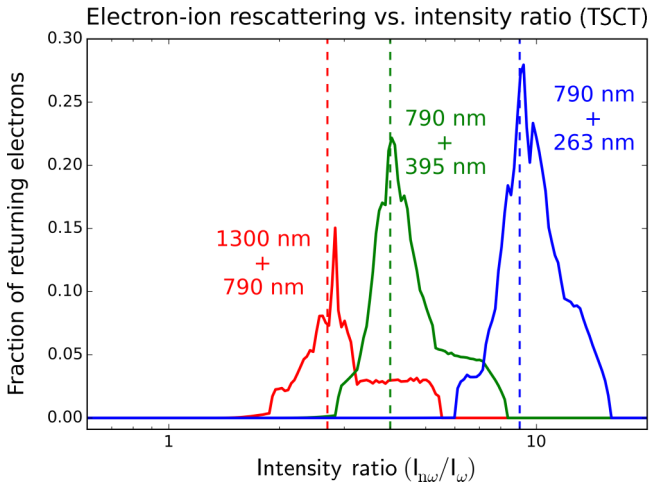

FIG. 14. The fraction of electrons that pass within 0.05 nm on the parent ion, plotted for two-color counter-rotating fields at various driving laser wavelengths. Hard electron-ion rescattering is optimized when the U_P of the fields are the same. In each case, the vertical lines indicate the intensity ratio that provides equal U_P for the two fields.

where equal intensities give equal ponderomotive energies, and describe a linearly polarized field. Importantly, this result suggests that efficient rescattering (and therefore HHG) can occur even with small amounts of longer-wavelength light. Since nonlinear frequency conversion processes are typically inefficient, two-color HHG schemes based on frequency downconversion—rather than upconversion—should be especially successful.

[1] P. Agostini, F. Fabre, G. Mainfray, G. Petite, and N. K. Rahman, Phys. Rev. Lett. **42**, 1127 (1979).

[2] D. D. Hickstein, P. Ranitovic, S. Witte, X.-M. Tong, Y. Huismans, P. Arpin, X. Zhou, K. E. Keister, C. W. Hogle, B. Zhang, C. Ding, P. Johnsson, N. Toshima, M. J. J. Vrakking, M. M. Murnane, and H. C. Kapteyn, Phys. Rev. Lett. **109**, 073004 (2012).

[3] A. Mcpherson, G. Gibson, H. Jara, U. Johann, T. S. Luk, I. A. McIntyre, K. Boyer, and C. K. Rhodes, J. Opt. Soc. Am. B **4**, 595 (1987).

[4] T. Popmintchev, M.-C. Chen, A. Bahabad, M. Gerrity, P. Sidorenko, O. Cohen, I. P. Christov, M. M. Murnane, and H. C. Kapteyn, Proc. Natl. Acad. Sci. USA **106**, 10516 (2009).

[5] M.-C. Chen, P. Arpin, T. Popmintchev, M. Gerrity, B. Zhang, M. Seaberg, D. Popmintchev, M. M. Murnane, and H. C. Kapteyn, Phys. Rev. Lett. **105**, 173901 (2010).

[6] T. Popmintchev, M.-C. Chen, P. Arpin, M. M. Murnane, and H. C. Kapteyn, Nat. Photonics **4**, 822 (2010).

[7] T. Popmintchev, M.-C. Chen, D. Popmintchev, P. Arpin, S. Brown, S. Ališauskas, G. Andriukaitis, T. Balčiunas, O. D. Mücke, A. Pugzlys, A. Baltuška, B. Shim, S. E. Schrauth, A. Gaeta, C. Hernández-García, L. Plaja, A. Becker, A. Jaron-Becker, M. M. Murnane, and H. C. Kapteyn, Science **336**, 1287 (2012).

[8] M.-C. Chen, C. Mancuso, C. Hernández-García, F. Dollar, B. Galloway, D. Popmintchev, P.-C. Huang, B. Walker, L. Plaja, A. A. Jaroń-Becker, A. Becker, M. M. Murnane, H. C. Kapteyn, and T. Popmintchev, Proc. Natl. Acad. Sci. USA **111**, E2361 (2014).

[9] D . Popmintchev, C. Hernandez-Garcia, F. Dollar, C. Mancuso, J. A. Perez-Hernandez, M.-C. Chen, A. Hankla, X. Gao, B. Shim, A. L. Gaeta, M. Tarazkar, D. A. Romanov, R. J. Levis, J. A. Gaffney, M. Foord, S. B. Libby, A. Jaron-Becker, A. Becker, L. Plaja, M. M. Murnane, H. C. Kapteyn, and T. Popmintchev, Science **350**, 1225 (2015).

[10] B. Zhang, D. F. Gardner, M. D. Seaberg, E. R. Shanblatt, H. C. Kapteyn, M. M. Murnane, and D. E. Adams, Ultramicroscopy **158**, 98 (2015).

[11] M. D. Seaberg, B. Zhang, D. F. Gardner, E. R. Shanblatt, M. M. Murnane, H. C. Kapteyn, and D. E. Adams, Optica **1**, 39 (2014).

[12] B. Zhang, M. D. Seaberg, D. E. Adams, D. F. Gardner, E. R. Shanblatt, J. M. Shaw, W. Chao, E. M. Gullikson, F. Salmassi, H. C. Kapteyn, and M. M. Murnane, Opt. Express **21**, 21970 (2013).

[13] S. Mathias, C. La-o-vorakiat, J. M. Shaw, E. Turgut, P. Grychtol, R. Adam, D. Rudolf, H. T. Nembach, T. J. Silva, M. Aeschlimann, C. M. Schneider, H. C. Kapteyn, and M. M. Murnane, J. Electron Spectrosc. Relat. Phenom. **189**, 164 (2013).

[14] E. Turgut, C. La-o-vorakiat, J. M. Shaw, P. Grychtol, H. T. Nembach, D. Rudolf, R. Adam, M. Aeschlimann, C. M. Schneider, T. J. Silva, M. M. Murnane, H. C. Kapteyn, and S. Mathias, Phys. Rev. Lett. **110**, 197201 (2013).

[15] C. La-O-Vorakiat, E. Turgut, C. A. Teale, H. C. Kapteyn, M. M. Murnane, S. Mathias, M. Aeschlimann, C. M. Schneider, J. M. Shaw, H. T. Nembach, and T. J. Silva, Phys. Rev. X **2**, 011005 (2012).

[16] K. M. Hoogeboom-Pot, J. N. Hernandez-Charpak, X. Gu, T. D. Frazer, E. H. Anderson, W. Chao, R. W. Falcone, R. Yang, M. M. Murnane, H. C. Kapteyn, and D. Nardi, Proc. Natl. Acad. Sci. USA **112**, 4846 (2015).

[17] C. I. Blaga, J. Xu, A. D. DiChiara, E. Sistrunk, K. Zhang, P. Agostini, T. A. Miller, L. F. DiMauro, and C. D. Lin, Nature **483**, 194 (2012).

[18] J. Xu, C. I. Blaga, K. Zhang, Y. H. Lai, C. D. Lin, T. A. Miller, P. Agostini, and L. F. DiMauro, Nat. Commun. **5**, 4635 (2014).

[19] P. B. Corkum, Phys. Rev. Lett. **71**, 1994 (1993).

[20] B. Yang, K. J. Schafer, B. Walker, K. C. Kulander, P. Agostini, and L. F. DiMauro, Phys. Rev. Lett. **71**, 3770 (1993).

[21] B. Walker, B. Sheehy, L. F. DiMauro, P. Agostini, K. J. Schafer, and K. C. Kulander, Phys. Rev. Lett. **73**, 1227 (1994).

[22] H. Eichmann, A. Egbert, S. Nolte, C. Momma, B. Wellegehausen, W. Becker, S. Long, and J. K. McIver, Phys. Rev. A **51**, R3414(R) (1995).

[23] S. Long, W. Becker, and J. K. McIver, Phys. Rev. A **52**, 2262 (1995).

[24] D. B. Milošević, W. Becker, and R. Kopold, Phys. Rev. A **61**, 063403 (2000).

[25] D. B. Milošević and W. Becker, Phys. Rev. A **62**, 011403(R) (2000).

[26] A. Rundquist, C. G. Durfee, Z. Chang, C. Herne, S. Backus, M. M. Murnane, and H. C. Kapteyn, Science **280**, 1412 (1998).

[27] A. Fleischer, O. Kfir, T. Diskin, P. Sidorenko, and O. Cohen, Nat. Photonics **8**, 543 (2014).

[28] O. Kfir, P. Grychtol, E. Turgut, R. Knut, D. Zusin, D. Popmintchev, T. Popmintchev, H. Nembach, J. M. Shaw, A. Fleischer, H. Kapteyn, M. Murnane, and O. Cohen, Nat. Photonics **9**, 99 (2015).

[29] D. D. Hickstein, F. J. Dollar, P. Grychtol, J. L. Ellis, R. Knut, C. Hernández-García, D. Zusin, C. Gentry, J. M. Shaw, T. Fan, K. M. Dorney, A. Becker, A. Jaroń-Becker, H. C. Kapteyn, M. M. Murnane, and C. G. Durfee, Nat. Photonics **9**, 743 (2015).

[30] T. Fan, P. Grychtol, R. Knut, C. Hernandez-Garcia, D. Hickstein, C. Gentry, C. Hogle, D. Zusin, K. Dorney, O. Shpyrko, O. Cohen, O. Kfir, L. Plaja, A. Becker, A. Jaron-Becker, M. M. Murnane, H. C. Kapteyn, and T. Popmintchev, in *CLEO: 2015 Postdeadline Paper Digest* (OSA, Washington, DC, 2015), p. JTh5C.1.

[31] T. Fan, P. Grychtol, R. Knut, C. Hernández-García, D. D. Hickstein, D. Zusin, C. Gentry, F. J. Dollar, C. A. Mancuso, C. W. Hogle, O. Kfir, D. Legut, K. Carva, J. L. Ellis, K. M. Dorney, C. Chen, O. G. Shpyrko, E. E. Fullerton, O. Cohen,

P. M. Oppeneer *et al.*, Proc. Natl. Acad. Sci. USA **112**, 14206 (2015).
[32] E. Hasović, W. Becker, and D. B. Milošević, Opt. Express **24**, 6413 (2016).
[33] C. A. Mancuso, D. D. Hickstein, P. Grychtol, R. Knut, O. Kfir, X.-M. Tong, F. Dollar, D. Zusin, M. Gopalakrishnan, C. Gentry, E. Turgut, J. L. Ellis, M.-C. Chen, A. Fleischer, O. Cohen, H. C. Kapteyn, and M. M. Murnane, Phys. Rev. A **91**, 031402 (R) (2015).
[34] A. Ferré, C. Handschin, M. Dumergue, F. Burgy, A. Comby, D. Descamps, B. Fabre, G. A. Garcia, R. Géneaux, L. Merceron, E. Mével, L. Nahon, S. Petit, B. Pons, D. Staedter, S. Weber, T. Ruchon, V. Blanchet, and Y. Mairesse, Nat. Photonics **9**, 93 (2015).
[35] A. D. Bandrauk and H. Z. Lu, Phys. Rev. A **68**, 043408 (2003).
[36] K.-J. Yuan and A. D. Bandrauk, Phys. Rev. A **92**, 063401 (2015).
[37] A. D. Bandrauk and K.-J. Yuan, in *From Atomic to Mesoscale: The Role of Quantum Coherence in Systems of Various Complexities*, edited by S. A. Malinovskaya and I. Novikova (World Scientific, Singapore, 2015).
[38] The TSCT is based on the simpleman's model, described in B. van Linden van den Heuvell and H. G. Muller, in *Multiphoton Processes*, edited by S. J. Smith and P. L. Knight, Vol. 8, Cambridge Studies of Modern Optics (Cambridge University Press, Cambridge, 1988), p. 25.
[39] A. T. J. B. Eppink and D. H. Parker, Rev. Sci. Instrum. **68**, 3477 (1997).
[40] C. Smeenk, L. Arissian, A. Staudte, D. M. Villeneuve, and P. B. Corkum, J. Phys. B: At., Mol. Opt. Phys. **42**, 185402 (2009).
[41] S. van der Walt, J. L. Schönberger, J. Nunez-Iglesias, F. Boulogne, J. D. Warner, N. Yager, E. Gouillart, and T. Yu, PeerJ **2**, e453 (2014).
[42] A. C. Kak and M. Slaney, *Principles of Computerized Tomographic Imaging* (IEEE Press, New York, 1988).
[43] W. Becker, F. Grasbon, R. Kopold, D. B. Milošević, G. G. Paulus, and H. Walther, Adv. At., Mol. Opt. Phys. **48**, 35 (2002).
[44] G. G. Paulus, W. Nicklich, H. Xu, P. Lambropoulos, and H. Walther, Phys. Rev. Lett. **72**, 2851 (1994).
[45] C. I. Blaga, F. Catoire, P. Colosimo, G. G. Paulus, H. G. Muller, P. Agostini, and L. F. DiMauro, Nat. Phys. **5**, 335 (2009).
[46] L. Guo, S. S. Han, X. Liu, Y. Cheng, Z. Z. Xu, J. Fan, J. Chen, S. G. Chen, W. Becker, C. I. Blaga, A. D. DiChiara, E. Sistrunk, P. Agostini, and L. F. DiMauro, Phys. Rev. Lett. **110**, 013001 (2013).
[47] T. Zuo, A. D. Bandrauk, and P. B. Corkum, Chem. Phys. Lett. **259**, 313 (1996).
[48] C. D. Lin, A.-T. Le, Z. Chen, T. Morishita, and R. Lucchese, J. Phys. B: At., Mol. Opt. Phys. **43**, 122001 (2010).
[49] J. Xu, C. I. Blaga, A. D. DiChiara, E. Sistrunk, K. Zhang, Z. Chen, A.-T. Le, T. Morishita, C. D. Lin, P. Agostini, and L. F. DiMauro, Phys. Rev. Lett. **109**, 233002 (2012).
[50] M. G. Pullen, B. Wolter, A.-T. Le, M. Baudisch, M. Hemmer, A. Senftleben, C. D. Schröter, J. Ullrich, R. Moshammer, C. D. Lin, and J. Biegert, Nat. Commun. **6**, 7262 (2015).
[51] B. Walker, B. Sheehy, K. C. Kulander, and L. F. DiMauro, Phys. Rev. Lett. **77**, 5031 (1996).
[52] M. V. Ammosov, N. B. Delone, and V. P. Krainov, Sov. Phys. JETP **64**, 1191 (1986).
[53] C. J. Joachain, N. J. Kylstra, and R. M. Potvliege, *Atoms in Intense Laser Fields* (Cambridge University Press, Cambridge, 2012).
[54] E. Hasović, M. Busuladžić, A. Gazibegović-Busuladžić, D. B. Milošević, and W. Becker, Laser Phys. **17**, 376 (2007).
[55] E. Hasović, A. Kramo, and D. B. Milošević, Eur. Phys. J.: Spec. Top. **160**, 205 (2008).
[56] W. Becker and D. B. Milošević, J. Phys. B: At., Mol. Opt. Phys. **48**, 151001 (2015).
[57] A. Kramo, E. Hasović, D. B. Milošević, and W. Becker, Laser Phys. Lett. **4**, 279 (2007).
[58] S. Odžak and D. B. Milošević, Phys. Rev. A **92**, 053416 (2015).
[59] N. B. Delone and V. P. Krainov, J. Opt. Soc. Am. B **8**, 1207 (1991).
[60] K. Radhakrishnan and A. C. Hindmarsh, *Description and Use of* LSODE, *the Livermore Solver for Ordinary Differential Equations* (NASA, Washington, DC, 1993).
[61] A. C. Hindmarsh, in *Scientific Computing: Applications of Mathematics and Computing to the Physical Sciences*, edited by R. S. Stapleman (North-Holland Publishing Company, Amsterdam, 1983).
[62] T. E. Oliphant, Comput. Sci. Eng. **9**, 10 (2007).
[63] X.-M. Tong and Shih-I Chu, Phys. Rev. A **58**, R2656(R) (1998).
[64] X. M. Tong, K. Hino, and N. Toshima, Phys. Rev. A **74**, 031405(R) (2006).